Editors' Suggestion | Featured in Physics

Active Nematic Flows over Curved Surfaces

Samuel Bell,[1,*] Shao-Zhen Lin,[2,*] Jean-François Rupprecht,[2] and Jacques Prost[1,3,†]
[1]Laboratoire Physico-Chimie Curie, UMR 168, Institut Curie, PSL Research University, CNRS, Sorbonne Université, 75005 Paris, France
[2]Aix Marseille Université, Université de Toulon, CNRS, Centre de Physique Théorique, Turing Center for Living Systems, 13288 Marseille, France
[3]Mechanobiology Institute, National University of Singapore, 117411 Singapore

(Received 11 March 2022; accepted 20 July 2022; published 6 September 2022)

Cell monolayers are a central model system in the study of tissue biophysics. In vivo, epithelial tissues are curved on the scale of microns, and the curvature's role in the onset of spontaneous tissue flows is still not well understood. Here, we present a hydrodynamic theory for an apical-basal asymmetric active nematic gel on a curved strip. We show that surface curvature qualitatively changes monolayer motion compared with flat space: the resulting flows can be thresholdless, and the transition to motion may change from continuous to discontinuous. Surface curvature, friction, and active tractions are all shown to control the flow pattern selected, from simple shear to vortex chains.

DOI: 10.1103/PhysRevLett.129.118001

Had Gaudi been a developmental biologist rather than an architect, he might have said that there are no flat epithelial tissues in nature. Tissue flows occur in the intrinsically curved environments encountered during morphogenetic processes or inner organs' self-renewal, e.g., in the gut, where flows of cells occur along a curvature gradient [1,2]. Yet, for practical reasons, most *in vitro* studies on collective epithelial tissue flows were performed on flat surfaces. These verified several predictions of active nematic theory, which, applied to tissue, predicts the relations between mechanical stress, flows, and cell shape fields, defined through a coarse-grained procedure [3–6].

Here, motivated by recent developments in 3D micropatterning and live-3D imaging techniques [7], we investigate theoretically the emergence of spontaneous flows within a covariant active nematic framework for epithelial tissues.

The effect of curvature on active nematics was explored in several recent studies [8–10] that extended previous equilibrium frameworks [11–14]. These theories are quadratic in the curvature tensor. Yet, epithelial tissues, which have lumen and substrate facing sides—called apical and basal, respectively, permit a linear coupling to curvature. Indeed, a body of recent work has shown that the underlying substrate curvature regulates the cellular architecture [15–17], with cells' orientation depending on the substrate convexity or concavity, both at the single cell [16,18,19] or collective tissue scale level [20–24]. Theoretical models that do consider such apico-basal asymmetry [25–27] do not, however, address the possibility of a mechanical feedback loop between flows and active stresses.

Here we show that, by affecting the cell orientation, the sign and intensity of the curvature alters the nature of the transition to flows in confined active nematic geometry and, in stark contrast to the noncurved case, can lead to thresholdless shear flows at vanishing activity or confinement size.

We first derive an active nematic hydrodynamic framework in the presence of up-down asymmetry within a curved manifold. We then predict new cell-shape and tissue flows patterns within monolayers placed on curved substrates. We show that there exists a critical curvature value above which a uniform state becomes unstable, distorts, and starts to flow. The flow mode depends on the magnitude and sign of the curvature. Then, we numerically show the existence of a discontinuous transition in the value of the flow velocity between these previously identified modes, as well as more complicated 2D modes such as vortex chains. We also highlight the existence of multiple steady state patterns in regions of the phase diagram previously thought to be stable.

We start by describing a fully developed active nematic phase with a unit-length director field $\boldsymbol{n}$. Surfaces are characterized by both the metric tensor g_{ij}, and the extrinsic curvature tensor C_i^j [28]. For convenience, we write an effective free energy $F = F_0 + F_C$, and define the molecular field $h_i = -\delta F/\delta n^i$, the functional derivative of the total free energy, with $(h_\perp,\ h_\parallel)$ those components respectively perpendicular and parallel to the director field $\boldsymbol{n}$. F has a part analogous to the Frank free energy of classic liquid crystals: $F_0 = \int dS[K_1(\nabla_j n^j)^2/2 + K_3(n^j\nabla_j n_i)^2/2 - h_\parallel^0 n_i n^i/2]$, where $dS = \sqrt{g}dx^1dx^2$, K_1, and K_3 are the splay and bend elastic moduli respectively, and $h_\parallel^0$ is the Lagrange multiplier enforcing the constraint $\boldsymbol{n}^2 = 1$. In this Letter, we use the one-constant approximation $K_1 = K_3 = K$ [29], motivated by recent observations in epithelial

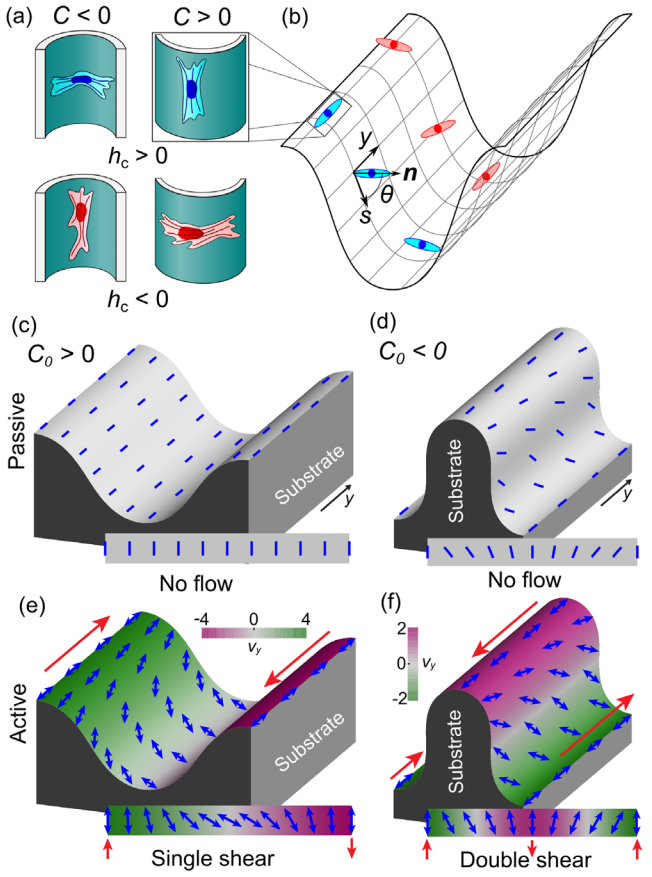

FIG. 1. (a) Cells with alignment parameter $h_c > 0$ in the free energy (blue cells, e.g., fibroblasts [16]), will align along the direction with the most negative (or least positive) curvature, whereas cells with $h_c < 0$ (red cells, e.g., MDCK cells [16]) will align oppositely. (b) The surface geometry: a strip, infinite in y, with curvature in the transverse s direction $C_{ss} = C_0 \cos 2\pi s/L$, where L is transverse contour length and $C_0 > 0$, showing single cells aligning according to their alignment parameter. (c)–(f) Typical cell orientation and velocity patterns of (c) passive uniform pattern, (d) passive nonuniform pattern, (e) active single shear flow pattern and (f) active double shear flow pattern. The color code refers to v_y, and the red arrows indicate flow directions. Cartesian plots of the orientation and velocity are given in the Supplemental Material, Fig. S1 [31].

tissues [30]. All ∇_i terms refer to covariant derivatives. We use Einstein notation for summation over repeated indices.

Here, we consider a linear curvature free energy,

$$F_C = \frac{1}{2}\int dS\, h_c C_i^j n^i n_j, \tag{1}$$

which is the simplest first order expansion in the curvature field allowed by nematic symmetry. If $h_c > 0$, cells prefer to align parallel to directions of greatest negative curvature, and perpendicular to directions of greatest positive curvature, and vice versa for $h_c < 0$; see Fig. 1(a).

The monolayer's velocity with respect to a fixed substrate $\boldsymbol{v}$ enters into tensors for the strain rate $u_i^j = (\nabla_i v^j + \nabla^j v_i - \nabla_k v^k g_i^j)/2$, and vorticity $\omega_i^j = (\nabla_i v^j - \nabla^j v_i)/2$. For simplicity, we assume incompressibility, $\nabla \cdot \boldsymbol{v} = 0$. The stress constitutive equation reads $\sigma_i^j = -P g_i^j + \tilde{\sigma}_i^j + \sigma_i^{Aj} + \sigma_i^{aj}$ for active gels [4], where P collects all the isotropic stresses; $\tilde{\sigma}_i^j = 2\eta u_i^j + (\nu/2)(n_i h^j + n^j h_i - n_k h^k g_i^j)$, where η is the kinematic viscosity, and ν is the shear alignment coefficient; $\sigma_i^{Aj} = -(n_i h^j - n^j h_i)/2$; and $\sigma_i^{aj} = -\zeta(n_i n^j - g_i^j/2)$ is the active stress [32]. The equation for the evolution of the director field reads as

$$\frac{Dn_i}{Dt} = \frac{h_i}{\gamma} - \nu u_i^j n_j + \nu_c C_i^j n_j, \tag{2}$$

where $Dn_i/Dt = \partial n_i/\partial t + v^j \nabla_j n_i + \omega_i^j n_j$ is the corotational derivative of the director field n_i; ν is the shear alignment coefficient. The last term of Eq. (2) is an active term different from the terms generated by the coupling in the effective free energy. We explore the role of this term in the Supplemental Material [31], Fig. S3; in the main text figures we set $\nu_c = 0$.

The force balance between internal stresses and momentum exchanges with the substrate reads as

$$\nabla^j \sigma_{ji} = \xi v_i + \lambda_b n^j \nabla_j n_i + \lambda_s n_i \nabla_j n^j, \tag{3}$$

where ξ is a substrate friction coefficient; λ_b (resp. λ_s) is an active bend (resp. splay) coefficient, expressing that an active nematic can specifically extract momentum from the substrate for bend or splay conformations [33,34]. In Eq. (3), we refrain from introducing a curvature-dependent friction for the sake of simplicity. The sum $\lambda_s + \lambda_b$ combination of these terms simply amounts to a shift in the overall value of the active stress ζ. Their difference, $\lambda_s - \lambda_b$, has no bulk counterpart in classical active gel theory [32]. It has been recently considered, but only within unbound domains [33].

We focus here on the geometry of an infinite strip of width L [Fig. 1(a)]. For in-plane curvilinear coordinates (s, y), $C_{ss}(s) = C_0 \cos ks$ is the only nonzero component of the curvature tensor, with C_0 being the curvature magnitude and $k = 2\pi/L$. In the spirit of Voituriez *et al.* [35], we first assume that the flow and orientation patterns are invariant along the y direction. Coupled with the incompressibility condition, this y invariance of the system implies that $v_s = 0$. Thus, the force balance in the s direction defines the pressure P. We need only consider one off diagonal stress component: σ_{sy}. We write σ_{sy}, the force balance, and Eq. (2), in terms of the molecular field components $(h_\perp, h_\parallel)$ and the director field angle θ [see Fig. 1(b)], such that $\boldsymbol{n} = (\cos\theta, \sin\theta)$ (Supplemental Material [31], Sec. I). The y-invariant system admits two uniform nonmoving solutions at steady state, $\theta = 0$ and

$\theta = \pi/2$, depending on the boundary conditions. Here, we focus on the homogeneous alignment condition (observed in experiments [6]) which permits one uniform solution, $\theta = \pi/2$ (the director field aligned parallel to the boundaries).

We first analyze the linear stability of a perturbation to the uniform state, $\delta\theta = \theta - \pi/2$, with boundary conditions $\delta\theta(0) = \delta\theta(L) = 0$. In the zero friction $\xi = 0$ limit and with stress-free boundary conditions $\sigma_{sy}(0) = \sigma_{sy}(L) = 0$, the force balance in the y direction can be integrated to give $\sigma_{sy} = -\lambda_s \delta\theta$. Replacing σ_{sy} in the stress equation shows that the active splay renormalizes the contractility, $\zeta \to \zeta + \lambda_s \equiv \zeta_s$. The curvature free energy coefficient is also renormalized, $h_c \to h_c - \tilde{\eta}\nu_c \equiv \tilde{h}_c$, where $\tilde{\eta} = 4\eta\gamma/[\gamma(\nu+1)^2 + 4\eta]$ is an effective viscosity. Introducing adimensional units $\tilde{s} = ks/2, \tau = (Kk^2/4\tilde{\eta})t$, the dynamical equation for the perturbation $\delta\theta$ can be written (Supplemental Material [31], Sec. II) as

$$\frac{\partial \delta\theta}{\partial \tau} = \left(-\frac{2\zeta_s(\nu+1)\tilde{\eta}}{Kk^2\eta} - \frac{4\tilde{h}_c C_0}{Kk^2}\cos 2\tilde{s} \right)\delta\theta + \frac{\partial^2 \delta\theta}{\partial \tilde{s}^2}, \qquad (4)$$

or $\dot{\delta\theta} = \mathcal{L}(\tilde{s})\delta\theta$, where $\mathcal{L}(\tilde{s})$ is the operator of the Mathieu equation $\mathcal{L}(\tilde{s}) = (a - 2q\cos 2\tilde{s}) + \partial_{\tilde{s}}^2$ [36]. The eigenvalues and eigenfunctions of this operator, $\mathcal{L}(\tilde{s})\phi_m = \lambda_m \phi_m$ [36], determine the stability of the system; since $\dot{\phi}_m = \lambda_m \phi_m$, any $\lambda_m > 0$ implies that the uniform solution is unstable. For $\delta\theta(0) = \delta\theta(L) = 0$, the eigenvalues are related to the odd characteristic numbers $b_m(q)$ of the Mathieu equation [36]. The lowest eigenfunction ϕ_1 is a single shear (SS) pattern, akin to Fig. 1(e). The second eigenfunction ϕ_2 is a double shear (DS) pattern, as in Fig. 1(f), where two shear bands are stitched together in the center of the strip. For a continuous transition from the nonflowing (NF) state to a single shear state, the lowest mode must vanish:

$$\lambda_1(q) = -\frac{\zeta_s(\nu+1)\tilde{\eta}L^2}{2\pi^2\eta K} + b_1(q) = 0. \qquad (5)$$

We found an excellent agreement between Eq. (5) and numerical simulations throughout the (C_0, ζ_s, L) phase space (Fig. 2 and the Supplemental Material [31]).

For small values of curvature $q = 2\tilde{h}_c C_0/Kk^2 \ll 1$, the expansion $b_1(q) \sim 1 + q$ yields the following curvature threshold for flow:

$$\frac{\tilde{h}_c C_{0,cr}}{2K} = \left(\frac{\pi}{L}\right)^2 + \frac{\zeta_s(\nu+1)\tilde{\eta}}{2\eta K}. \qquad (6)$$

Such approximation of the critical curvature $C_{0,cr}$ agrees well with simulations [Supplemental Material [31], Fig. S2(a)]. When $C_0 = 0$, Eq. (6) reduces to that of the active Fredericksz transition found in Ref. [35]. As shown

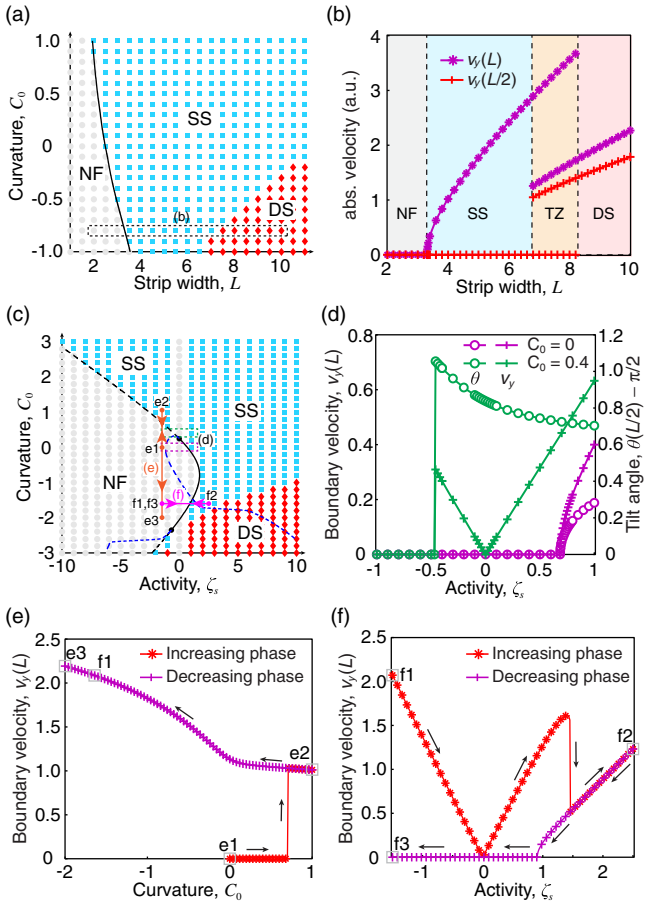

FIG. 2. Flow patterns and transitions in the zero friction limit ($\xi = 0$) obtained from numerical simulations (Supplemental Material [31], Sec. I). (a) C_0–L flow pattern diagram for $\zeta_s = 4$: no flow (gray, NF); single shear (blue, SS); and double shear (red, DS), and analytical prediction [Eq. (5)] of the continuous NF-SS transition (black solid curve). (b) Constant $C_0 = -0.8$ cut through (a) (the dotted box) showing continuous NF-SS transition, and discontinuous SS-DS transition. (c) ζ_s–C_0 flow pattern diagram and analytical prediction [Eq. (5)] of the NF-SS transition (solid, continuous; dashed, discontinuous). The two black circular spots separate the continuous transition and the discontinuous transition. The blue dashed curve represents the discontinuous SS-NF (or SS-SS) transition while increasing (or decreasing) ζ_s from a SS pattern (see Supplemental Material [31], Fig. S7). The parameter paths $e1$-$e2$-$e3$ (e) and $f1$-$f2$-$f3$ (f) are quenching simulations, as shown in (e),(f). Diagrams in (a),(c) are obtained from an initial NF state. (d) Constant C_0 cuts [$C_0 = 0$ and $C_0 = 0.4$, dashed boxes in (c)] showing a discontinuous NF-SS transition for the curved case, with thresholdless flows around zero activity. (e) Pattern selection upon varying C_0 quasistatically [orange path in (c); see Supplemental Material [31], Sec. I.D] with $\zeta_s = -1.5$. See also Supplemental Material [31], Movie S1. (f) Pattern selection upon varying ζ_s quasistatically [magenta path in (c); see Supplemental Material [31], Sec. I.D] with $C_0 = -1.6$. See also Supplemental Material [31], Movie S2. The initial SS state ($f1$) was prepared through quenching of C_0 [see the point ($f1$) in (c) and (e)]. Parameters other than ξ are those in the Supplemental Material [31], Table 1, including $\nu_c = 0$, $\zeta = 0$, and $\lambda_b = 0$.

in Eq. (6), the curvature field induces a new length scale, $(2K/\tilde{h}_c C_0)^{1/2}$, which pits the cost of nonalignment with the curvature against the cost of director field deformations. As in flat space [6,35], increasing the strip width L can induce a continuous NF-SS transition [Figs. 2(a) and 2(b)]. For fixed L, the NF-SS threshold is a nonmonotonic function of the curvature [see Fig. 2(c)]; such behavior, which contrasts with the linear relation Eq. (6), is a consequence of the higher-order terms in the $b_1(q)$ expansion at larger q.

Our simulations also reveal transitions to higher-order shear modes, each differentiated by their velocities in the center $v_y(L/2)$ and the edge $v_y(L)$ of the strip: $v_y(L/2) = v_y(L) = 0$ for NF; $v_y(L/2) = 0$, $v_y(L) \neq 0$ for SS; and $v_y(L/2)$, $v_y(L) \neq 0$ for DS. In particular, the DS pattern emerges for $\tilde{h}_c C_0 < 0$ [see Figs. 2(a) and 2(c)]. When $\tilde{h}_c C_0 > 0$, cells in the center of the strip prefer to align toward $\theta = 0$; the central portion is biased toward a large perturbation from $\theta = \pi/2$, favoring the SS pattern. When $\tilde{h}_c C_0 < 0$, this is reversed. The cells in the center of the strip prefer to align toward $\theta = \pi/2$, favoring the DS pattern. There is no direct NF-DS transition for $\xi = 0$; see Fig. 2(b). The SS-DS transition is discontinuous, with a transition zone of metastability.

We find that the NF-SS transition is not always continuous [see Fig. 2(d) and Supplemental Material [31], Fig. S5]. At two tricritical points [the black dots in Fig. 2(c)], the transition changes from continuous (solid black line) to discontinuous (dashed black line). The upper tricritical point occurs right at $\zeta_s = 0$; see Fig. 2(c) and the Supplemental Material [31], Fig. S5. Close to the lower tricritical point, the growth rates of the SS and DS modes are nearly degenerate, $\lambda_1 \approx \lambda_2$. A higher-order analysis of a mixed state in this region shows that couplings between the shear modes can effectively reverse the sign of the third order term of the amplitude equation (Supplemental Material [31], Sec. II), a typical hallmark of a tricritical point, offering excellent agreement with the numerical simulations.

We then explored the regimes of hysteresis along the discontinuous NF-SS transition upon performing a quasistatic variation of the curvature (Fig. 2). Indeed, the NF-SS transition and the SS-NF transition occur at different values of C_0; see Fig. 2(e) and the Supplemental Material [31], Fig. S6 and Movie S1. The lines of these transitions are known as the spinodal lines. The boundary of linear stability of the NF state $\lambda_1 = 0$ gives one of these spinodal lines for each tricritical point. To find the other spinodals [the blue dashed lines in Fig. 2(c)], we prepare a single shear state and then transform the system quasistatically (varying C_0 or ζ_s) until the shear state has lost absolute stability [Fig. 2(f); Supplemental Material [31], Sec. I, Fig. S7, and Movie S2]. We note that the upper blue spinodal line crosses $C_0 = 0$, implying that a single shear state can be at least metastable in flat space for both signs of ζ_s. Such a behavior is a departure from the established work on the continuous active shear transition in flat strips [35].

We find that the $\zeta_s = 0$ line cuts through the domain of stability of the single shear patterns. There, curvature destabilises the uniform director field pattern [see Eq. (6) and Figs. 1(c) and 1(d)]. The resulting orientation gradients drive motion even for arbitrarily small active stresses, and the flow velocity scales linearly as $v_y \propto \zeta_s$; see Fig. 2(d). Similar thresholdless active flows are found in Ref. [37] as a consequence of the constraints imposed by the anchoring condition.

When friction is nonzero, there is no tidy equation in $\delta\theta$. We expand in Fourier space and find that the spatial dependence of the curvature field leads to mode coupling (Supplemental Material [31], Sec. II). We find the critical curvature $C_{0,cr}$ for small curvature values:

$$\frac{h_\xi C_{0,cr}}{2K} = \left(\frac{\pi}{L}\right)^2 \left(1 + \frac{(\nu+1)\zeta_s}{2K[\xi/\gamma + (\pi/L)^2(\eta/\tilde{\eta})]}\right), \quad (7)$$

where we define a renormalized curvature-coupling coefficient: $h_\xi = h_c - \nu_c[\xi + \eta(\pi/L)^2]/(\xi/\gamma + \pi^2\eta/L^2\tilde{\eta})$. Equation (7) shows excellent agreement with numerical

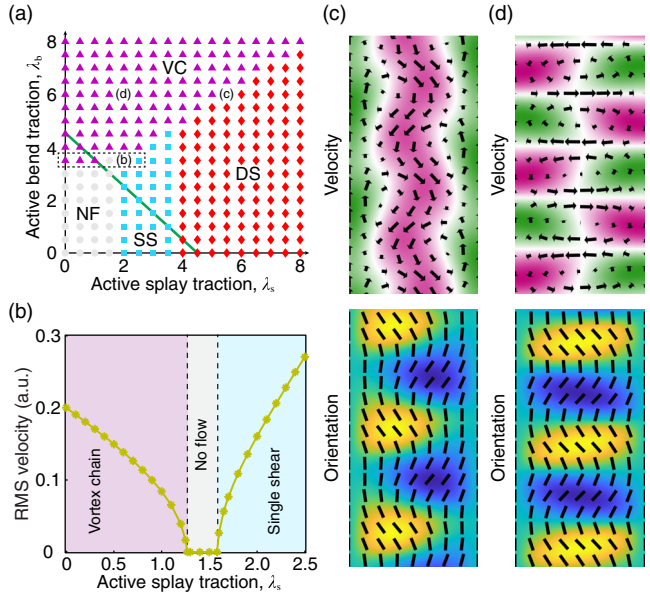

FIG. 3. The effect of active bend traction λ_b. Results shown here were obtained from full 2D simulations. (a) Phase diagram of the flow patterns [stable (light gray); single shear (blue); double shear (red) and vortex chain (magenta)] with respect to the active splay traction λ_s and the active bend traction λ_b. (b) Phase transition regulated by the active splay traction λ_s, which corresponds to the horizontal dash box in (a) with $\lambda_b = 3.5$. (c),(d) The perturbed double shear flow pattern (c) and the vortex chain pattern (d), which correspond to the dataset shown in (a). In the velocity map, the color code represents v_y and arrows denote velocity vectors; in the orientation map, the color code refers to θ and lines for orientation directors. Parameters: $\xi = 0.6$, $L = 8$, and $C_0 = 0$.

simulations [Supplemental Material [31], Fig. S2(b)] and matches Eq. (6) for a vanishing substrate friction $\xi = 0$. Higher absolute curvatures are needed to initiate flows with larger friction; see the Supplemental Material [31], Fig. S2(b). In contrast to the zero friction case, we find a direct and continuous transition from the nonflowing to double shear patterns; see the Supplemental Material [31], Fig. S9.

To check the assumption of y invariance, we perform two-dimensional simulations (Supplemental Material, Sec. I [31]). For $\lambda_b = 0$, the assumption holds very well [Fig. 3(a) and Supplemental Material [31], Fig. S10]. However, for large enough active bend traction $\lambda_b > 0$, longitudinal instabilities appear [Fig. 3(c)], eventually leading to a vortex chain pattern [Fig. 3(d) and Supplemental Material [31], Fig. S12] [38]. The vortex chain state shares a phase boundary with the NF, SS, and DS patterns [Fig. 3(a)]. Recalling that the sum of the active bend and splay correspond to a bulk renormalization of the contractility, $\zeta \to \zeta + (\lambda_s + \lambda_b)/2$, we can consider systems of equal contractility by taking diagonal cuts of Fig. 3(a) such as the green line. For a given value of the contractility, we may observe each of the four flow patterns, depending on the ratio between the active splay and bend tractions.

Perspectives.—In this Letter, we have traveled beyond the existing paradigm of continuous transition to flows in confined active nematics [35]. The introduction of a curvature field allows for tight control of a wider variety of flow structures than simple shear states, each with unique biological significance (e.g., a double shear flow permits net transport for weak anchoring boundary conditions). Further, by suppressing the threshold to motion, curvature vastly increases the range of tissue parameters that allow for flows. Finally, our findings of discontinuous transitions and hysteresis offer new perspectives on tissue dynamics: even transient mechanical perturbations, such as a brief shock to the tissue, may lead to long-term changes from a quiescent state to a spontaneously flowing one. This concept that living matter, epithelial tissues included, could exist with hair triggers to motion has the potential to transform our understanding of morphogenesis, cancer spreading, or biofilm growth.

S. B. and J. P. are funded by the Human Frontiers in Science Program (HFSP RGP0038/2018) and acknowledge useful discussions with other members of the project. J.-F. R. and S-Z. L. are funded by the Investissements d'Avenir French Government program managed by the French National Research Agency (ANR-16-CONV-0001 and ANR-17-CE13-0032 COVFEFE) and the A*MIDEX Excellence Initiative of Aix-Marseille University.

*These authors contributed equally to this work.
†Jacques.Prost@curie.fr

[1] E. Hannezo, J. Prost, and J.-F. Joanny, Phys. Rev. Lett. **107**, 078104 (2011).
[2] A. E. Shyer, T. Tallinen, N. L. Nerurkar, Z. Wei, E. S. Gil, D. L. Kaplan, C. J. Tabin, and L. Mahadevan, Science **342**, 212 (2013).
[3] S. Ramaswamy, R. A. Simha, and J. Toner, Europhys. Lett. **62**, 196 (2003).
[4] M. C. Marchetti, J.-F. Joanny, S. Ramaswamy, T. B. Liverpool, J. Prost, M. Rao, and R. A. Simha, Rev. Mod. Phys. **85**, 1143 (2013).
[5] T. B. Saw, A. Doostmohammadi, V. Nier, L. Kocgozlu, S. Thampi, Y. Toyama, P. Marcq, C. T. Lim, J. M. Yeomans, and B. Ladoux, Nature (London) **544**, 212 (2017).
[6] G. Duclos, C. Blanch-Mercader, V. Yashunsky, G. Salbreux, J.-F. Joanny, J. Prost, and P. Silberzan, Nat. Phys. **14**, 728 (2018).
[7] W. Xi, J. Saleh, A. Yamada, C. Tomba, B. Mercier, S. Janel, T. Dang, M. Soleilhac, A. Djemat, H. Wu, B. Romagnolo, F. Lafont, R.-M. Mège, Y. Chen, and D. Delacour, Biomaterials **282**, 121380 (2022).
[8] D. J. G. Pearce, P. W. Ellis, A. Fernandez-Nieves, and L. Giomi, Phys. Rev. Lett. **122**, 168002 (2019).
[9] D. J. Pearce, New J. Phys. **22**, 063051 (2020).
[10] G. Napoli and S. Turzi, Phys. Rev. E **101**, 022701 (2020).
[11] P. Biscari and E. M. Terentjev, Phys. Rev. E **73**, 051706 (2006).
[12] S. Kralj, R. Rosso, and E. G. Virga, Soft Matter **7**, 670 (2011).
[13] G. Napoli and L. Vergori, Phys. Rev. E **85**, 061701 (2012).
[14] G. Napoli and L. Vergori, Phys. Rev. E **94**, 020701(R) (2016).
[15] D. Baptista, L. Teixeira, C. van Blitterswijk, S. Giselbrecht, and R. Truckenmüller, Trends Biotechnol. **37**, 838 (2019).
[16] S. J. P. Callens, R. J. C. Uyttendaele, L. E. Fratila-Apachitei, and A. A. Zadpoor, Biomaterials **232**, 119739 (2020).
[17] N. Harmand, A. Huang, and S. Hénon, Phys. Rev. X **11**, 031028 (2021).
[18] J. Comelles, D. Caballero, R. Voituriez, V. Hortigüela, V. Wollrab, A. L. Godeau, J. Samitier, E. Martínez, and D. Riveline, Biophys. J. **107**, 1513 (2014).
[19] N. D. Bade, T. Xu, R. D. Kamien, R. K. Assoian, and K. J. Stebe, Biophys. J. **114**, 1467 (2018).
[20] C. Liu, J. Xu, S. He, W. Zhang, H. Li, B. Huo, and B. Ji, J. Mech. Behav. Biomed. Mater. **88**, 330 (2018).
[21] L. Pieuchot, J. Marteau, A. Guignandon, T. Dos Santos, I. Brigaud, P.-F. Chauvy, T. Cloatre, A. Ponche, T. Petithory, P. Rougerie, M. Vassaux, J.-L. Milan, N. Tusamda Wakhloo, A. Spangenberg, M. Bigerelle, and K. Anselme, Nat. Commun. **9**, 3995 (2018).
[22] S.-M. Yu, B. Li, F. Amblard, S. Granick, and Y.-K. Cho, Biomaterials **265**, 120420 (2021).
[23] S.-M. Yu, J. M. Oh, J. Lee, W. Lee-Kwon, W. Jung, F. Amblard, S. Granick, and Y.-K. Cho, Acta Biomater. **77**, 311 (2018).
[24] M. Luciano, S.-L. Xue, W. H. De Vos, L. Redondo-Morata, M. Surin, F. Lafont, E. Hannezo, and S. Gabriele, Nat. Phys. **17**, 1382 (2021).
[25] M. Dicko, P. Saramito, G. B. Blanchard, C. M. Lye, B. Sanson, and J. Étienne, PLoS Comput. Biol. **13**, e1005443 (2017).
[26] S. J. Streichan, M. F. Lefebvre, N. Noll, E. F. Wieschaus, and B. I. Shraiman, eLife **7**, e27454 (2018).
[27] R. G. Morris and M. Rao, Phys. Rev. E **100**, 022413 (2019).

[28] G. Salbreux and F. Jülicher, Phys. Rev. E **96**, 032404 (2017).
[29] P.-G. De Gennes and J. Prost, *The Physics of Liquid Crystals* (Oxford University Press, New York, 1993), 83.
[30] C. Blanch-Mercader, P. Guillamat, A. Roux, and K. Kruse, Phys. Rev. Lett. **126**, 028101 (2021).
[31] See Supplemental Material at http://link.aps.org/supplemental/10.1103/PhysRevLett.129.118001 for further details of the calculations and numerical simulations.
[32] J. Prost, F. Jülicher, and J.-F. Joanny, Nat. Phys. **11**, 111 (2015).
[33] A. Maitra, P. Srivastava, M. C. Marchetti, J. S. Lintuvuori, S. Ramaswamy, and M. Lenz, Proc. Natl. Acad. Sci. U.S.A. **115**, 6934 (2018).
[34] Here we will neglect possible curvature-gradient active forces, which would lead to an extra term $\lambda_C \nabla_j C_i^j$ in Eq. (3).
[35] R. Voituriez, J.-F. Joanny, and J. Prost, Europhys. Lett. **70**, 404 (2005).
[36] NIST Digital Library of Mathematical Functions, edited by f. W. J. Olver, A. B. Olde Daalhuis, D. W. Lozier, B. I. Schneider, R. F. Boisvert, C. W. Clark, B. R. Miller, B. V. Saunders, H. S. Cohl, and M. A. McClain, http://dlmf.nist.gov/, Release 1.0.28 of 2020-09-15.
[37] R. Green, J. Toner, and V. Vitelli, Phys. Rev. Fluids **2**, 104201 (2017).
[38] A. Doostmohammadi, M. F. Adamer, S. P. Thampi, and J. M. Yeomans, Nat. Commun. **7**, 10557 (2016).